Journal of Colloid and Interface Science 431 (2014) 50–63

Contents lists available at ScienceDirect

Journal of Colloid and Interface Science

www.elsevier.com/locate/jcis

Mixing enhancement of low-Reynolds electro-osmotic flows in microchannels with temperature-patterned walls

A. Alizadeh, L. Zhang, M. Wang *

Department of Engineering Mechanics and CNMM, Tsinghua University, Beijing 100084, China

ARTICLE INFO

Article history:
Received 28 April 2014
Accepted 31 May 2014
Available online 12 June 2014

Keywords:
Electro-osmotic flow
Lattice Boltzmann method
Mixing enhancement
Temperature-patterned walls
Thermo-electrochemical migration phenomenon

ABSTRACT

Mixing becomes challenging in microchannels because of the low Reynolds number. This study aims to present a mixing enhancement method for electro-osmotic flows in microchannels using vortices caused by temperature-patterned walls. Since the fluid is non-isothermal, the conventional form of Nernst–Planck equation is modified by adding a new migration term which is dependent on both temperature and internal electric potential gradient. This term results in the so-called thermo-electrochemical migration phenomenon. The coupled Navier–Stokes, Poisson, modified Nernst–Planck, energy and advection–diffusion equations are iteratively solved by multiple lattice Boltzmann methods to obtain the velocity, internal electric potential, ion distribution, temperature and species concentration fields, respectively. To enhance the mixing, three schemes of temperature-patterned walls have been considered with symmetrical or asymmetrical arrangements of blocks with surface charge and temperature. Modeling results show that the asymmetric arrangement scheme is the most efficient scheme and enhances the mixing of species by 39% when the Reynolds number is on the order of 10^{-3}. Current results may help improve the design of micro-mixers at low Reynolds number.

© 2014 Elsevier Inc. All rights reserved.

1. Introduction

In the recent decades, the rapid advancement of MEMS has made it possible to integrate the multi-functional micro devices on a chip (Lab-On-a-Chip) for biological and biochemical uses. One of the most common elements used as a main part of MEMS devices is micro-mixer. Appropriate and controllable mixing of species in these devices is of great importance for scientific research and applications. At small scale, the flows mostly remain in laminar regime through micro-channels, which makes diffusion as the main mechanism of mixing. As a result, one may have to design long enough microchannels for appropriate mixing of species. Therefore, control of mixing and mixing enhancement in microchannels has been of great interest in recent years [1].

Various designs and studies are conducted to increase convection in mixing enhancement. Passive micro-mixers are designed with specific geometry features in order to increase the chaotic flow regime. Previous studies and schemes include three dimensional serpentine mixers [2–4], zigzag or waveform mixers [5], staggered herringbone mixers [6], micro-mixers with patterned blocks [7], parallel lamination of micro-mixers with the basic of T-mixer or Y-mixer [8]. However, difficulty in manufacturing microchannels with designed specific geometric features poses limitation on the use of passive schemes. On the other hand, micro-mixers based on active mixing enhancement methods are designed in such a way that the external mechanical or electrical forces cause the chaotic flow pattern. In fact, these forces generate transverse flows through the microchannel. The external mechanical forces could be implemented, for instance, by pressure disturbance methods such as serial segmentation [9], pressure disturbance along the microchannel [10] and integrated micro-stirrer in the mixing channel [11]. For the electrical forces, they could be implemented by electro-hydrodynamic disturbance, dielectrophoretic disturbance and electrokinetic disturbance methods [12]. Several studies have been conducted to reveal the mechanism of these forces in the micro-mixers. These studies have shown that by specifying the operating conditions, the active mixing strategies yield an efficient species mixing as a result of the repeated stretching and folding of the sample streams at the interface between them [1,13].

In recent years, the electrokinetically driven flow techniques in MEMS devices enable us to manipulate the flow regimes and as a result, enhance the mixing of species sample. Wang et al. [14] showed that in an electrokinetically driven flow such as electro-osmotic flow, the mixing enhancement effect for the interlaced

* Corresponding author.
E-mail address: mrwang@tsinghua.edu.cn (M. Wang).

http://dx.doi.org/10.1016/j.jcis.2014.05.070
0021-9797/© 2014 Elsevier Inc. All rights reserved.

arrangement of zeta potential-patterned walls is higher than that for symmetrical arrangement. Tang et al. [15] and Coleman and Sinton [16] showed that through applying a periodically varying electric field to the side channels of a T-/cross-shaped micro-mixer, the species could be injected alternately into the main microchannel. The time-dependent external electric field and the effects of this scheme on the mixing enhancement have been the research subject of some literatures [17,18]. They have demonstrated that, for instance, with sinusoidally alternating external electric fields, the flow field could emerge as a wavy-flow pattern.

Electrokinetic flows have significant parameters such as temperature gradient which could be used as a key resource for active control of mixing in these type flows. Alizadeh et al. [19] showed that by applying a temperature difference between inlet flow and walls of a microchannel, one can control vortex scales formed in the flow field. It was shown that the temperature gradient changed the ion distribution. Consequently, the net electric charge density and as a result the electrical body force are redistributed in such a way according to the ion distribution [20].

As mentioned above, mixing enhancement of species in micro-mixers has emerged as one of the challenging subjects in MEMS. In the present study, the temperature field is used as an external-like source to change the ion distribution and electrical body force [19]. Compared with our previous work [19], this work will present a modified Nernst–Planck equation which could properly model the ions species electrodynamic transport in non-isothermal fluids. This modification allows us to investigate the impacts of temperature gradient in both transverse and longitudinal direction of micro-channel. The problem is formulated by solving the Poisson equation for internal electric potential field, modified Nernst–Planck equation for ion distribution, Navier–Stokes equation for flow field, advection–diffusion equation for species concentration and energy equation for temperature distribution. Since the governing equations are coupled together, they are solved by an iterative process. In this work, the coupled lattice Boltzmann methods are used to solve the governing equations numerically. The Navier–Stokes, Poisson–Nernst–Planck equations for ions species distribution and the advection–diffusion equation for species concentration are solved using the multiple lattice Boltzmann methods [21] and the energy equation is solved using a model for thermal evolution equation with generalized heat source term [22].

2. Problem definition

Fig. 1 shows three schematic designs of micro-mixers with patterned temperature and zeta potential walls. In Fig. 1, red, blue and red–blue blocks represent parts of the microchannel walls with different amounts of T and ψ. Micro-mixer schemes A and B consist of two types of blocks ($red\,block \equiv T = T_{wall}, \psi = \zeta_{wall}$; $blue\,block \equiv T = T_{in}, \psi = 0$) while micro-mixer scheme C, in addition to red and blue blocks, has a third type block, red–blue block ($red - blue\,block \equiv T = T_{in}, \psi = \zeta_{wall}$). Meanwhile, in micro-mixer schemes B and C, the red blocks are placed in a symmetric arrangement while in scheme A they are placed in an asymmetric arrangement. In order to study the distribution of ions species and electrical body force along the width of the micro-mixers, we defined two planes named plane A and B which are placed in $x/H = 2.0$ and $x/H = 2.2$, respectively (Fig. 1). The EOF studied in this paper is an electrolyte flow through a two dimensional microchannel with length L and width H. The inlet electrolyte is kept at constant temperature T_{in} while $T_{in} < T_{wall}$. The fluid motion is caused by both external electric field with strength E_x applied by use of an Anode and a Cathode placed at the two ends of the microchannel and pressure gradient. The ratio of length to width of this microchannel (L/H) is equal to 5 and the electrolyte considered here is symmetric and has a 1:1 ionic ratio ($|Z_+| = |Z_-| = Z = 1$). In this study, it is assumed that the microchannel is made of PDMS, and the electrolyte is a dilute solution of NaCl.

In order to characterize the relative size of the thickness of electric double layer (EDL), the dimensionless parameter κ is defined as $\kappa = KH = H/\lambda$ with H representing the channel width and λ the Debye length calculated by:

$$\lambda = K^{-1} = \sqrt{\frac{\varepsilon_0 \varepsilon_r K_B T_{wall}}{2Z^2 e^2 n_{i\infty}}} \tag{1}$$

where T_{wall}, as mentioned in Fig. 1, is the red block temperature used as the reference temperature. Here, by selecting the value of κ and H, the value of ion concentration, $n_{i\infty}$, is determined. Sometimes, instead of $n_{i\infty}$ the amount of molar concentration, c, is also determined. In such cases, the molar concentration in K mol/m^3 is calculated as $c = n_{i\infty}/(1000N_A)$, where N_A is the Avogadro constant. Other physical parameters such as μ, ε_r and k are only functions of temperature and assumed constant for a given temperature. The values of these quantities for $T = 19.85$ °C (=293 K) are presented in Table 1.

To study the effects of temperature gradients on the flow field and as a result mixing enhancement of species, we used two set amount of temperatures on the blocks as $T_{wall} = 87.5$ °C, $T_{in} = 12.5$ °C and $T_{wall} = 31.25$ °C, $T_{in} = 25$ °C. Moreover, the amount of zeta potential on the red and blue blocks was kept constant as $\zeta = -50$ mv and $\zeta = 0$ mv, respectively. Considering species concentration, it is assumed that at the inlet of micro-mixers we implemented species boundary condition as $y/H \geqslant 0.5 \rightarrow C_s = 1$ and $y/H < 0.5 \rightarrow C_s = 0$.

3. Mathematical models

3.1. Navier–Stokes equations

For a Newtonian fluid at microscale without any mass source and in laminar flow regime, the conventional continuity and Navier–Stokes equations are still valid as [23]:

$$\begin{aligned} &(a) \quad \tfrac{\partial \rho}{\partial t} + \nabla \cdot (\rho \boldsymbol{u}) = 0 \\ &(b) \quad \tfrac{\partial (\rho \boldsymbol{u})}{\partial t} + \boldsymbol{u} \cdot \nabla (\rho \boldsymbol{u}) = -\nabla p + \nabla \cdot [\nu \nabla (\rho \boldsymbol{u})] + \boldsymbol{F} \end{aligned} \tag{2}$$

where ρ (kg/m^3) is the density of the electrolyte, $\boldsymbol{u}$ (m/s) is the flow velocity vector, t (s) time, p (Pa) fluid pressure, ν (m^2/s) the kinetic viscosity and $\boldsymbol{F}$ (N/m^3) is the body force density which may include all the implemented body forces such as electrical body force or pressure gradient. In cases that the fluid is incompressible, the pressure gradient could be included in $\boldsymbol{F}$. As a result, while in this study the pressure gradient is considered in some case of micro-mixer types, so one can define the body force as:

$$\boldsymbol{F} = \boldsymbol{F_e} + \boldsymbol{F_p} = -\rho_e(\nabla \varphi + \nabla \psi) + \nabla P \tag{3}$$

where $\nabla \varphi$ is the external electric potential field and in this study we have $-(\nabla \varphi)_x = E_x, (\nabla \varphi)_y = 0$, $\nabla \psi$ is the internal electric potential field which we ignored the impact of $(\nabla \psi)_y$ due to the low ion concentration dissolved in electrolyte [19].

Boundary conditions governing Navier–Stokes equations for three micro-mixer schemes are as follows:

$$\begin{aligned} &\textit{for red, blue and red} - \textit{blue blocks}: \\ &y = 0 \;\rightarrow\; u = v = 0, y = H \;\rightarrow\; u = v = 0 \\ &\textit{for inlet and outlet}: \\ &x = 0 \;\rightarrow\; \frac{\partial u}{\partial x} = \frac{\partial v}{\partial x} = 0, p = P_{atm} \\ &x = l \;\rightarrow\; \frac{\partial u}{\partial x} = \frac{\partial v}{\partial x} = 0, p = P_{atm} \end{aligned} \tag{4}$$

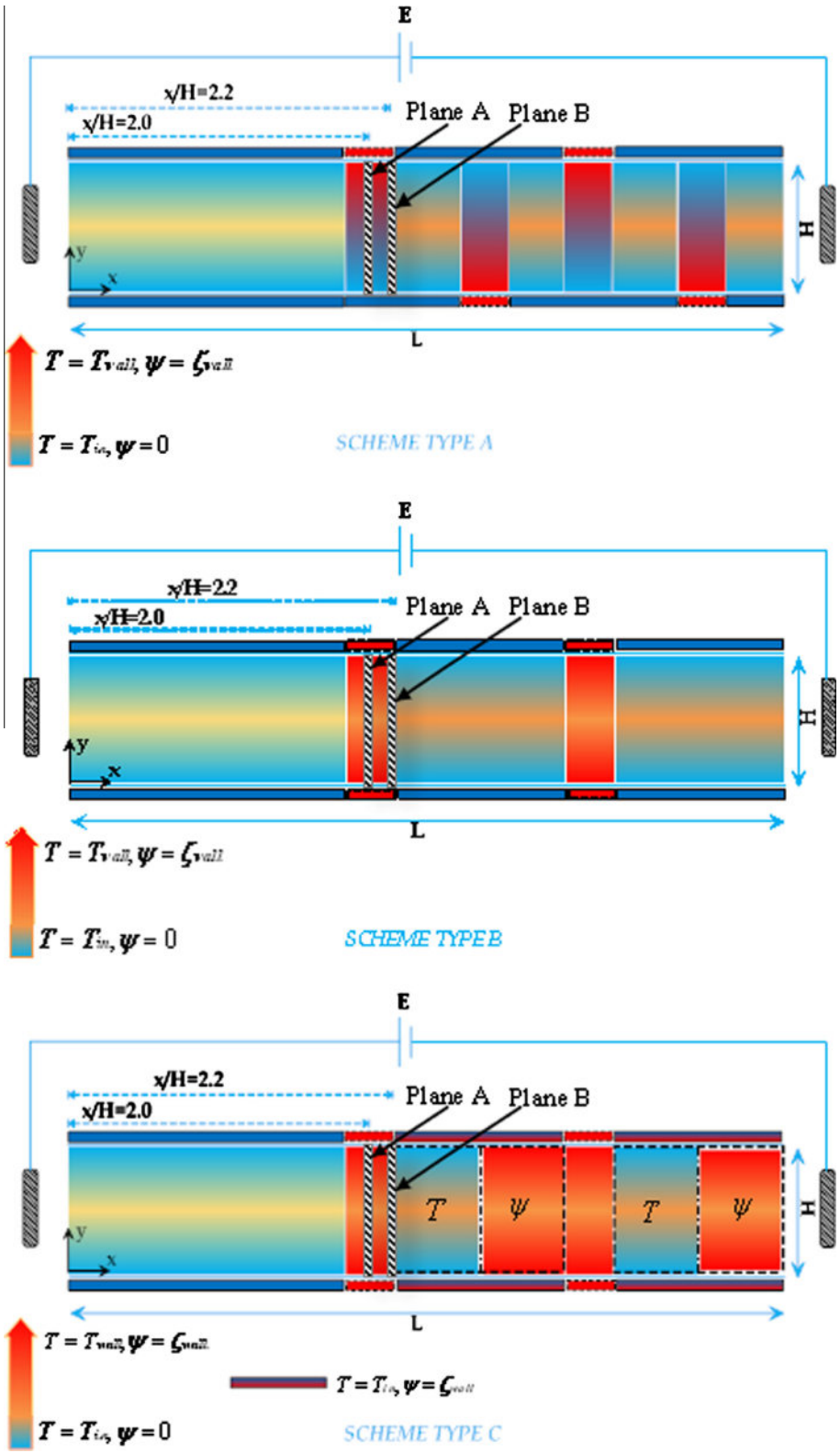

Fig. 1. Three scheme of micro-mixers with temperature and zeta potential patterned blocks in symmetric and asymmetric arrangement.

3.2. Modified Nernst–Planck equation

The mass conservation equation for *i*th ion species in an electrolyte could be written in general form as [24]:

$$\frac{\partial C_i}{\partial t} + \nabla \cdot \mathbf{J}_i + \lambda_i C_i = R_i \tag{5}$$

where C_i demonstrates the *i*th ionic concentration, $\mathbf{J_i}$ denotes the species flux, λ_i a radioactive decay constant and R_i presents the rate at which the *i*th ions is produced or consumed by chemical reactions. In the present study, the terms of radioactive decay constant and the rate of producing or consuming of ions are neglected. However, $\mathbf{J_i}$ the flux of *i*th ions consists of advection, diffusion and

Table 1
Properties and parameters at T = 19.85 °C (=293 K).

Variable	Value (unit)
H	6×10^{-6} m
e	1.602×10^{-19} c
K_B	1.381×10^{-23} j/k
$n_{i\infty}$	6.022×10^{20} ion/m^3
ε_r	80
ε_0	8.854×10^{-12} C/(V × m)
ρ	1000 kg/m^3
μ	1×10^{-3} Pa × s
c_p	4180 j/(kg × K)
k	0.613 W/(m × K)
$D_{Na^+} = D_{Cl^-}$	10^{-9} m^2/s
D_s	10^{-10} m^2/s

dispersion terms. Neglecting the dispersion, one can denote the flux of ions in the form of [24]:

$$\boldsymbol{J}_i = -\left(\frac{eZ_iD_i}{KT}\right)C_i\nabla\psi - D_i(\nabla C_i) + C_i\boldsymbol{u} \tag{6}$$

where the first term on the right hand side denotes the electrochemical migration, the second term to ions diffusion and the last term to advective transport. This is the famous Nernst–Planck equation. In the ions flux equation, e, Z_i, D_i, K and T are denoted as the absolute charge of electron, valance number for ith ion, diffusion coefficient for ith ion, Boltzmann constant and the absolute temperature, respectively. Wang and Kang [21] presented the electrodynamic transport process equation for ions in electrokinetic flows for isothermal incompressible uniform fluids with no polarization, radiation or chemical reactions. Introducing Eq. (6) into Eq. (5) leads to the ions electrodynamic transport equation:

$$\frac{\partial C_i}{\partial t} + \boldsymbol{u}\cdot\nabla C_i = D_i\nabla^2 C_i + \frac{eZ_iD_i}{KT}\nabla\cdot(C_i\nabla\psi) \tag{7}$$

Eq. (7) is no longer valid for fluids with non-zero temperature gradient. Introducing Eq. (6) into Eq. (5) and considering the fact that temperature is no longer constant in electrolyte, one can demonstrate the modified form of Nernst–Planck equation for fluids with non-zero temperature gradient as:

$$\frac{\partial C_i}{\partial t} + \boldsymbol{u}\cdot\nabla C_i = D_i\nabla^2 C_i + \frac{eZ_iD_i}{K}\left(\nabla\psi\cdot\nabla\left(\frac{C_i}{T}\right) + \frac{C_i}{T}\nabla^2\psi\right) \tag{8}$$

Rewriting Eq. (8) based on the conventional form of Nernst–Planck equation (Eq. (7)), eventually one can obtain the modified form of the Nernst–Planck equation as:

$$\frac{\partial C_i}{\partial t} + \boldsymbol{u}\cdot\nabla C_i = D_i\nabla^2 C_i + \frac{eZ_iD_i}{KT}\nabla\cdot(C_i\nabla\psi) - \frac{eZ_iD_iC_i}{KT^2}\nabla T\cdot\nabla\psi \tag{9}$$

where the third term in the right hand side of the equation represents the thermo-electrochemical migration term.

Boundary conditions for the Nernst–Planck equation is defined based on the Poisson–Boltzmann ion distribution equation ($C_i = n_{i\infty}\exp(-Z_ie\psi(x,y)/(K_BT_{mean}(x)))$) which is still valid near the walls of a microchannel due to the equilibrium state available in these regions. As a result, one can denote the ith ion concentration boundary conditions for micro-mixers as follows:

$$\begin{aligned}
&\textit{for red, blue and, red} - \textit{blue blocks}:\\
&y = 0 \textit{ and } y = H \;\rightarrow\; C_i = n_{i\infty}\exp\left(-\frac{Z_ie\psi}{K_BT}\right)\\
&\textit{for inlet and outlet}:\\
&x = 0 \;\rightarrow\; C_i = n_{i\infty}\\
&x = l \;\rightarrow\; \frac{\partial C_i}{\partial x} = 0
\end{aligned} \tag{10}$$

3.3. Poisson equation for internal electric potential field

The local internal electric potential field, ψ, which is caused by the ionic distribution and is governed by the Poisson equation, is as follows [25]:

$$\frac{\partial\psi}{\partial t} = \chi\left(\nabla^2\psi + \frac{\rho_e}{\varepsilon_r\varepsilon_0}\right) \tag{11}$$

where ε_0 is the permittivity of vacuum, ε_r is the local amount of electrolyte permittivity to vacuum permittivity and ρ_e denotes the local net electric charge density. χ is the electric potential diffusivity coefficient which is equal to unity in this simulation. Considering the definition of ρ_e as $\sum_i eZ_iC_i$, the electrical body force is calculated by using Eq. (3) as $\boldsymbol{F_e} = -\rho_e(\nabla\varphi + \nabla\psi)$.

Boundary conditions governing Eq. (11) for micro-mixer schemes is as:

$$\begin{aligned}
&\textit{for red and red} - \textit{blue blocks}:\\
&\psi = \zeta_{wall}\\
&\textit{for blue blocks}:\\
&\psi = 0\\
&\textit{for inlet and outlet}:\\
&x = 0 \;\rightarrow\; \psi = 0\\
&x = l \;\rightarrow\; \frac{\partial\psi}{\partial x} = 0
\end{aligned} \tag{12}$$

3.4. Species concentration equation

The governing equation on species concentration could be considered as Eq. (9) with assuming the electrochemical and thermo-electrochemical migrations equal to zero. So, the species concentration equation is denoted as [14]:

$$\frac{\partial C_s}{\partial t} + \boldsymbol{u}\cdot\nabla C_s = D_s\nabla^2 C_s \tag{13}$$

where C_s and D_s denote the species concentration and species diffusivity coefficient, respectively.

Boundary condition governing Eq. (13) is as follows:

$$\begin{aligned}
&\textit{for red, blue and red} - \textit{blue blocks}:\\
&y = 0 \textit{ and } y = H \;\rightarrow\; \frac{\partial C_s}{\partial y} = 0\\
&\textit{for inlet and outlet}:\\
&x = 0 \;\rightarrow\; \frac{y}{H} \geq 0.5 \;\rightarrow\; C_s = 1\\
&x = 0 \;\rightarrow\; \frac{y}{H} < 0.5 \;\rightarrow\; C_s = 0\\
&x = l \;\rightarrow\; \frac{\partial C_s}{\partial x} = 0
\end{aligned} \tag{14}$$

3.5. Energy equation

In the present work, heat source terms such as Joule heating or any external heat sources are assumed negligible, and therefore the energy equation, the governing equation on temperature field, could be described as [19]:

$$\frac{\partial T}{\partial t} + (\boldsymbol{u}\cdot\nabla T) = \frac{k}{\rho c_p}\nabla^2 T \tag{15}$$

where c_p and k denote the specific heat capacity and thermal conductivity of the electrolyte, respectively. The boundary conditions for the energy equation are as:

$$\begin{aligned}&\text{for red blocks}:\\&T = T_{wall}\\&\text{for blue and red}-\text{blue blocks}:\\&T = T_{in}\\&\text{for inlet and outlet}:\\&x = 0 \;\rightarrow\; T = T_{in}\\&x = l \;\rightarrow\; \frac{\partial T}{\partial x} = 0\end{aligned} \tag{16}$$

4. Numerical methods

The governing equations in the present work are solved by the coupled lattice Boltzmann methods. In this rather new numerical method for each of the governing equations, one evolution equation is defined as the equivalent governing equation in mesoscopic space. In this section, the evolution equation for each of the governing equations mentioned in Section 3 will be presented. It is noteworthy that in the present study, we consider the *D2Q9* lattice for discretizing the velocities. The direction system for *D2Q9* system is shown in Fig. 2.

4.1. Evolution equations

4.1.1. For hydrodynamics (Navier–Stokes equations)

The discrete Boltzmann density distribution equation for solving the Navier–Stokes equations in the presence of external forces is indicated as follows [26]:

$$f_i(\boldsymbol{X}+\boldsymbol{e_i}\delta_t, t+\delta_t) - f_i(\boldsymbol{X},t) = -\frac{1}{\tau_v}\left[f_i(\boldsymbol{X},t) - f_i^{eq}(\boldsymbol{X},t)\right] + \delta_t F_i \tag{17}$$

where index i is assigned values from 0 to 8 in the standard *D2Q9* lattice. f_i is the density distribution function at place X and time t. v is the kinematic viscosity which is related to the relaxation time τ_v as $v = (\tau_v - 0.5)C_s^2\delta_t$. C_s is the speed of sound in the fluid having relation with the speed of particles in the lattice $c = \delta_x/\delta_t$ as $C_s = c/\sqrt{3}$. F_i is the external force distribution function at the same time and place and defined as follows:

$$F_i = \frac{(-\nabla p + \rho_e \boldsymbol{E} - \rho_e \nabla\psi)\cdot(\boldsymbol{e_i}-\boldsymbol{u})}{\rho c^2} f_i^{\boldsymbol{eq}} \tag{18}$$

The Maxwell–Boltzmann equilibrium distribution function for Eqs. (17) and (18) is [27]:

$$f_i^{eq} = \omega_i \rho\left[1 + \frac{3(\boldsymbol{e_i}\cdot\boldsymbol{u})}{c^2} + \frac{9(\boldsymbol{e_i}\cdot\boldsymbol{u})^2}{2c^4} - \frac{3}{2}\frac{(\boldsymbol{u}\cdot\boldsymbol{u})}{c^2}\right] \tag{19}$$

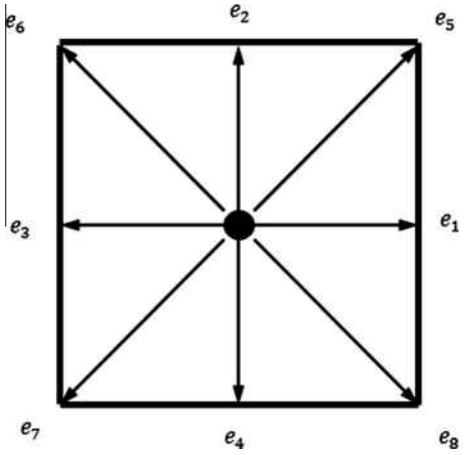

Fig. 2. *D2Q9* discrete velocities.

where $\boldsymbol{u}$ is the macroscopic velocity vector and ρ is the density of the fluid. ω_i represents the weighting factors for *D2Q9* lattice as follows:

$$\begin{aligned}&\omega_i = \frac{4}{9} \quad i = 0\\&\omega_i = \frac{1}{9} i = 1,2,3,4\\&\omega_i = \frac{1}{36} i = 5,6,7,8\end{aligned} \tag{20}$$

After evolution, the macroscopic values of the density, velocity and pressure are calculated as follows:

$$\rho = \sum_{i=0}^{8} f_i,\;\; \rho u = \sum_{i=0}^{8} f_i e_i,\;\; p = C_s^2\rho = \frac{\rho}{3} \tag{21}$$

4.1.2. For electrodynamics (Poisson equation)

The evolution equation for internal electrical potential in a 2D discrete lattice according to the Wang's model is written as follows [20]:

$$h_i(\boldsymbol{X}+\boldsymbol{e_i}\delta_{t,g}, t+\delta_{t,g}) - h_i(\boldsymbol{X},t) = -\left(\frac{1}{\tau_h}\right)\left[h_i(\boldsymbol{X},t) - h_i^{eq}(\boldsymbol{X},t)\right] + \delta_{t,h}\omega_i\left(1-\frac{0.5}{\tau_h}\right)\left(\frac{\rho_e}{\varepsilon_r\varepsilon_0}\right) \tag{22}$$

where h_i is the electric potential distribution function, $\boldsymbol{X}$ is the place vector, $\boldsymbol{e_i}$ is the microscopic velocity vector of the particles in *D2Q9* model, $\delta_{t,h}$ is the time step and here is equal to 1. τ_h is the dimensionless relaxation time which is defined as:

$$\tau_h = \frac{3\chi\delta_{t,h}}{2\delta_x^2} + 0.5 \tag{23}$$

where δ_x is the lattice constant and χ is the electric potential diffusivity coefficient which is equal to unity in this simulation. h_i^{eq} is the Maxwell–Boltzmann equilibrium distribution function for electric potential. The Maxwell–Boltzmann distribution function for Poisson–Boltzmann equation is:

$$h_i^{eq}(X,t) = \varpi_i\psi \tag{24}$$

where ϖ_i is the weight factor:

$$\varpi_i = \begin{Bmatrix} 0 & i=0\\ \frac{1}{6} & i=1,2,3,4\\ \frac{1}{12} & i=5,6,7,8\end{Bmatrix} \tag{25}$$

Finally, the macroscopic amount of the electric potential is calculated as:

$$\psi = \sum_{i=0}^{8}\left(h_i + \frac{0.5\delta_{t,h}\omega_i\rho_e}{\varepsilon_r\varepsilon_0}\right) \tag{26}$$

4.1.3. For heat transfer (energy equation)

According to assumptions mentioned in Section 3.5, in the present study internal heat sources such as Joule heating and viscous dissipation are negligible ($\dot{Q} = 0$). Therefore, whatever we have liquid or solid, the evolution equation can be generally given as [28]:

$$\theta_i(\boldsymbol{X}+\boldsymbol{e_i}\delta_t, t+\delta_t) - \theta_i(\boldsymbol{X},t) = -\left(\frac{1}{\tau_\theta}\right)\left[\theta_i(\boldsymbol{X},t) - \theta_i^{eq}(\boldsymbol{X},t)\right] + \omega_i\delta_{t,\theta}\left(1-\frac{0.5}{\tau_\theta}\right)\left(\frac{\dot{Q}}{\rho c_p}\right) \tag{27}$$

where θ_i is the internal energy distribution function and τ_θ is the dimensionless relaxation time as $\tau_\theta = \left(\frac{3}{2}\right)\left(\frac{\alpha}{c^2\delta_{t,\theta}}\right) + 0.5$. Clearly, $\dot{Q}$ is

the heat source term. The Maxwell–Boltzmann equilibrium function for Eq. (27) is as follows [28]:

$$\theta_i^{eq} = -\bar{\vartheta}_i T \frac{\boldsymbol{u}\cdot\boldsymbol{u}}{C^2} \quad i=0$$
$$\theta_i^{eq} = \bar{\vartheta}_i T\left[\frac{3}{2}+\frac{3\boldsymbol{e_i}\cdot\boldsymbol{u}}{2c^2}+\frac{9(\boldsymbol{e_i}\cdot\boldsymbol{u})^2}{2c^2}-\frac{3\boldsymbol{u}\cdot\boldsymbol{u}}{2c^2}\right] \quad i=1,2,3,4 \tag{28}$$
$$\theta_i^{eq} = \bar{\vartheta}_i T\left[3+\frac{\boldsymbol{e_i}\cdot\boldsymbol{u}}{c^2}+\frac{9(\boldsymbol{e_i}\cdot\boldsymbol{u})^2}{2c^2}-\frac{3\boldsymbol{u}\cdot\boldsymbol{u}}{2c^2}\right] \quad i=5,6,7,8$$

with

$$\bar{\vartheta}_i = \begin{Bmatrix} -\frac{2}{3} & i=0 \\ \frac{1}{9} & i=1,2,3,4 \\ \frac{1}{36} & i=5,6,7,8 \end{Bmatrix} \tag{29}$$

where T is the temperature of the fluid. The macroscopic value of the temperature is calculated as follows:

$$T = \sum_{i=0}^{i=8}\theta_i + \left(\frac{\delta_{t,\theta}}{2}\right)\left(\frac{\dot{Q}}{\rho c_p}\right) \tag{30}$$

4.1.4. For ion transport (modified Nernst–Planck equation)

Wang and Kang [21] presented the evolution equation to solve the ions transport in an isothermal electrolyte. In fact, the Nernst–Planck equation is an advection–diffusion equation with a source term for electrochemical migration of ions due to the internal electric potential field effects. Based on what mentioned in Section 3.2, the modified evolution equation for ions transport is presented as:

$$g_\alpha(\boldsymbol{X}+\boldsymbol{e_\alpha}\delta_{t,D_i}, t+\delta_{t,D_i}) - g_\alpha(\boldsymbol{X},t) = -\frac{1}{\tau_{D_i}}[g_\alpha(\boldsymbol{X},t)-g_\alpha^{eq}(\boldsymbol{X},t)]$$
$$+\omega_\alpha\delta_{t,D_i}\left(1-\frac{0.5}{\tau_{D_i}}\right)\left(\frac{eZ_iD_i}{KT}\nabla\cdot(C_i\nabla\psi)-\frac{eZ_iD_iC_i}{KT^2}\nabla T\cdot\nabla\psi\right) \tag{31}$$

where τ_{D_i} is the dimensionless relaxation time for the ith ion transport related to the diffusion coefficient D_i, and time step δ_{t,D_i}.

The dimensionless relaxation time is calculated as:

$$\tau_{D_i} = \frac{3D_i}{2C_{D_i}\delta_x} + 0.5 \tag{32}$$

The equilibrium distribution function for a $D2Q9$ lattice system is denoted as:

$$g_{\alpha=0}^{eq} = \frac{-2C_i}{3}\frac{\boldsymbol{u}\cdot\boldsymbol{u}}{C_{D_i}^2}$$
$$g_{\alpha=1,2,3,4}^{eq} = \frac{C_i}{9}\left[\frac{3}{2}+\frac{3\boldsymbol{e_i}\cdot\boldsymbol{u}}{2C_{D_i}^2}+\frac{9(\boldsymbol{e_i}\cdot\boldsymbol{u})^2}{2C_{D_i}^2}-\frac{3\boldsymbol{u}\cdot\boldsymbol{u}}{2C_{D_i}^2}\right] \tag{33}$$
$$g_{\alpha=5,6,7,8}^{eq} = \frac{C_i}{36}\left[3+\frac{3\boldsymbol{e_i}\cdot\boldsymbol{u}}{C_{D_i}^2}+\frac{9(\boldsymbol{e_i}\cdot\boldsymbol{u})^2}{2C_{D_i}^2}-\frac{3\boldsymbol{u}\cdot\boldsymbol{u}}{2C_{D_i}^2}\right]$$

where C_{D_i} denotes the lattice speed for ith ion separately and defined as:

$$C_{D_i} = \frac{\delta_x}{\delta_{t,D_i}} \tag{34}$$

It is worth mentioning that the diffusion lattice speed for ions transport, C_{D_i}, could be independent of diffusion lattice speed c in other evolution equations and assigned any positive amount while one can obtain the amount of τ_{D_i} in the range of $0.5 < \tau_{D_i} < 2$ [29].

Finally, the macroscopic amounts of ions are calculated by:

$$C_i = \sum g_\alpha + \frac{\delta_{t,D_i}}{2}\left(\frac{eZ_iD_i}{KT}\nabla\cdot(C_i\nabla\psi)-\frac{eZ_iD_iC_i}{KT^2}\nabla T\cdot\nabla\psi\right) \tag{35}$$

4.1.5. For species concentration (advection–diffusion equation)

Comparing modified Nernst–Planck equation (Eq. (9)) with the species concentration equation (Eq. (13)), it is concluded that the governing equation on species concentration is, in fact, the modified Nernst–Planck equation with zero valance number. Therefore, the evolution equation for species concentration could be considered as Eq. (31) with $Z_i = 0$. The dimensionless relaxation time and the equilibrium distribution function are obtained as the same as modified Nernst–Planck evolution equation by Eq. (32) and Eq. (33), respectively. It is worth mentioning that the macroscopic amount of species concentration is obtained by Eq. (35) while $Z_i = 0$.

4.2. Boundary treatment methods for lattice Boltzmann models

One of the challengeable subjects of study for the lattice Boltzmann methods is to present an approach in order to obtain the non-streamed distribution functions which are in fact the unknown distribution functions in boundaries. Since in this study we are solving the evolution equations for governing equations in coupled iterative methods, the consistency of boundary treatment methods is of great importance. In this section, we will introduce the second-order accuracy boundary treatment methods which were used in solving the governing evolution equations.

For hydrodynamics boundary conditions, we used the counter-slip method in order to obtain the unknown distribution functions in walls, inlet and outlet of micro-mixers [30]. For energy equation, we implemented the correcting coefficient method [31].

Several attempts have been performed in order to present consistent boundary condition method for advection–diffusion equations. In this study, we present a new approach for general types of boundary conditions for advection–diffusion equations with source terms. This method could be implemented easily to any kind of walls such as corners or even curved boundaries. It is noteworthy that this method and the D'Orazio's method [32], predict same unknown amounts of distribution functions on the stationary walls. This method is based on partitioning the distribution functions to known and unknown parts and then by introducing a correction factor (α), one can obtain an equilibrium amount (σ_0) based on known part of distribution functions and the correction factor. Eventually, with multiplying the related weighting factor in the unknown direction by the σ_0, the unknown distribution functions are obtained.

For instance, the upper wall unknown distribution functions are $\varepsilon_4, \varepsilon_7, \varepsilon_8$ which ε could be each of the modified Nernst–Planck, Poisson or advection–diffusion distribution functions. Considering the general form for obtaining the macro amounts as:

$$\sigma = \sum \epsilon_i + \eta \tag{36}$$

where η is the source term, one can partitioning it to two parts of known and unknown distribution functions as follows:

$$\epsilon_4+\epsilon_7+\epsilon_8 = \sigma_\Omega - \sigma_k - \eta \tag{37}$$

where σ_Ω is the macro amount of related variable at the boundary and σ_k is the sum of known amounts of distribution functions as:

$$\sigma_k = \epsilon_0+\epsilon_1+\epsilon_2+\epsilon_3+\epsilon_5+\epsilon_6 \tag{38}$$

Considering the sum of related weighting factor in the unknown distribution function directions for each evolution method, one can obtain the correcting factor as:

$$\alpha = \omega_4+\omega_7+\omega_8 \tag{39}$$

As a result, considering Eq. (37), σ_0 is obtained as follows:

$$\sigma_0 = \left(\frac{1}{\alpha}\right)(\epsilon_4+\epsilon_7+\epsilon_8) = \left(\frac{1}{\alpha}\right)(\sigma_\Omega-\sigma_k-\eta) \tag{40}$$

Finally, the unknown distribution functions are obtained as:

$$\begin{aligned}\epsilon_4 &= \omega_4\sigma_0\\ \epsilon_7 &= \omega_7\sigma_0\\ \epsilon_8 &= \omega_8\sigma_0\end{aligned} \tag{41}$$

Considering Eqs. (36)–(40), one can present a relation for σ_0 in general form for each type of boundary condition such as straight walls, curved boundaries or corners as follows:

$$\sigma_0 = \left(\frac{1}{\sum\omega_i}\right)[\sigma_\Omega - \sigma_k - \eta] \tag{42}$$

where $\sum\omega_i$ denotes the sum of related weighting factors in the direction of unknown distribution functions. Eventually, the unknown distribution functions are obtained as:

$$\epsilon_i = \omega_i\sigma_0 \tag{43}$$

4.3. Iterative scheme and convergence criteria

Based on what we mentioned in Section 1, the governing equations are coupled together and they should be solved in an iterative process. Fig. 3 shows the flow chart diagram of the iteration scheme which we used in this study. For each iteration, the distribution of internal electric potential field is solved until steady state based on the evolution equation which was mentioned in Section 4. Then, ion distribution is solved through the modified Nernst–Planck evolution equation (Eq. (31)). The net electric charge density is obtained from the ions distribution of the current iteration. The Navier–Stokes equation is solved in which the electrical body force is obtained from the results of Nernst–Planck as the previous equation in current iteration. Using the results of velocity field, one can solve the energy equation as the next equation. Finally, the species concentration is solved based on what has been obtained for velocity field in current iteration.

In order to achieve an accurate solution for this iterative process, we define four convergence criteria for internal electric potential field, velocity field, species concentration and energy equation as follows:

$$\varepsilon_{\delta=\psi,\mathbf{U},C_s,T} = \sqrt{\sum_{\mathbf{r}}\left(\frac{\delta^n(\mathbf{r}) - \delta^{n-1}(\mathbf{r})}{\delta^n(\mathbf{r})}\right)^2} \tag{44}$$

where n denotes the iteration number and $\mathbf{r}$ the location vector. The iteration will be stopped and the solution assumed to be as steady state when the amounts of ε are typically less than given error which is often equal to 1×10^{-6}.

5. Results and discussion

In this section, first, we validate the results of our coupled lattice Boltzmann methods for PNP and NS equations with available analytical solutions. For this purpose, the results of u, ψ and concentrations of Na^+ and Cl^- in cross section of the microchannel are presented. Second, the result of our code for solving a simple convection heat transfer is validated by the available analytical solution. Finally, the results of the micro-mixer schemes are studied.

5.1. Benchmarks

If we assume an isothermal EOF scenario in the microchannel which is fully developed in hydrodynamics and electrokinetics with constant amount of zeta potential on the walls, since the relation $|(Z_ie\zeta)/(K_BT)| \leqslant 1$ is valid, the Debye–Huckel approximation can be used and as a result an analytical solution for velocity,

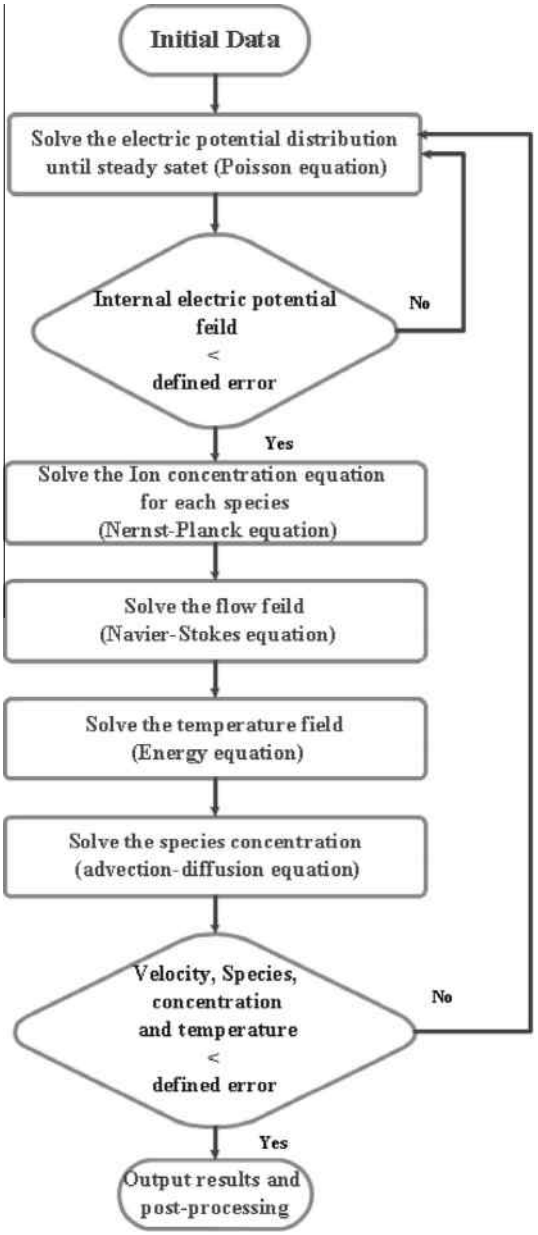

Fig. 3. Flow chart of iteration procedure for coupled lattice Boltzmann methods.

internal electric potential and ions species concentrations can be obtained as follows [33]:

$$\begin{aligned}&(a)\quad \frac{\psi}{\zeta} = \frac{\cosh\left(\kappa y - \frac{\kappa H}{2}\right)}{\cosh\left(\frac{\kappa H}{2}\right)}\\ &(b)\quad \left[1 - \frac{u}{U_{ref}}\right] = \frac{\cosh\left(\kappa y - \frac{\kappa H}{2}\right)}{\cosh\left(\frac{\kappa H}{2}\right)}\\ &(c)\quad C_i = n_{i\infty}\exp\left(-\frac{Z_ie\psi}{K_BT}\right)\end{aligned} \tag{45}$$

A lattice of 251×51 node is constructed in order to solve the coupled PNP and NS lattice Boltzmann methods. The dimensionless parameter of Debye length is $\kappa = H/\lambda = 5.93$ where $H = 6\times10^{-6}$ and the external electric field strength is $E_x = 1000$ V/m. The constant zeta potential on the walls of the microchannel is selected as $\zeta = -25$ mv. The diffusion coefficient of ion species is $D_i = 10^{-8}$ m^2/s and the ionic density is $n_{i\infty} = 6.022\times10^{19}$ ion/m^3. It is worth mentioning that we chose $n_{i\infty}$ in such a way to have higher amount of Debye length in order to valid our code for solving the PNP + NS when the Debye length is considerable compared with the

microchannel width. Fig. 4 shows a good agreement between analytical and lattice Boltzmann coupled methods results. Consequently, the capability of our code to solve the coupled PNP and NS equations is validated. The code for solving the energy equation is as the same as the validated structure code which we presented in our previous work [19].

5.2. Mixing enhancement and micro-mixer schemes

In this section, the quantitative results and discussion of mixing enhancement of species, ions species concentration distribution, flow field and electrical body force are presented for micro-mixers which were mentioned in Section 2. For each micro-mixer scheme, we consider two set of temperature differences and two Reynolds numbers. For all micro-mixer schemes, the amount of κ is equal to 18.7. The electrolyte motion could be caused by both electrical body force (due to external electric field and net electric charge density) and pressure gradient. The upper and lower walls of these microchannels could be kept at various heterogeneous models of charge and temperature amount. It is worth mentioning that the inlet electrolyte is kept at T_{in} for all micro-mixer schemes. Due to the presence of two kinds of body force (electrical body force and pressure gradient), we would be able to define two reference velocities as:

$$U_{ref,electric} = -\frac{\varepsilon_0 \varepsilon_r E_x \zeta}{\mu}$$
$$U_{ref,pressure} = -\frac{\nabla P \times H^2}{12 \times \rho \nu} \quad (46)$$

Fig. 5 shows streamline patterns and contour of species for micro-mixer scheme A in which E denotes the strength of external electric field, ∇P the pressure gradient and $\Delta T = (T_{wall} - T_{in})/T_{in}$ the non-dimensional definition for temperature difference between red and blue blocks of the microchannel. Obviously, this scheme is designed based on an asymmetric arrangement of blocks (red blocks) with $\zeta = \zeta_{wall} = -50$ mv and $T = T_{wall}$ all the while the rest of walls (blue blocks) have $\zeta = 0$ and $T = T_{in}$. From now on, the red and red–blue blocks which have constant non-zero charges are called activator blocks, while the neutral blocks assigned to those blue blocks with zero amount of charge. Considering the definition of reference velocities for both electrical body force and pressure gradient (Eq. (46)), we could define the Reynolds number as:

$$Re = \frac{(U_{ref,electric} + U_{ref,pressure})H}{\nu} \quad (47)$$

As a result, the Reynolds number for Fig. 5a and b is $Re = 1.08 \times 10^{-3}$ and Fig. 5c and d is $Re = 1.0642 \times 10^{-2}$.

Fig. 5a shows the micro-mixer scheme A with implementing both electrical and pressure gradient body forces to the electrolyte due to external electric field $E = 5 \times 10^3$ V/m and pressure gradient $\nabla P = 10^3$ N/m^3. It is shown that in the boundary region of red and blue blocks, four vortices form near the microchannel walls. In other word, the streamline pattern indicates that a y-directional force drives the flow to the walls near red block region and as a result a chaotic-like flow pattern is generated.

Fig. 5b shows the micro-mixer in Fig. 5a when ΔT increases. Comparing Fig. 5a with 5b, it is found that the generality of the flow pattern of micro-mixer Fig. 5a is still preserved while the vortices scale becomes larger and as a result the flow regime emerges as a powerful chaotic pattern flow. Consequently, one can expect that the mixing of species would be enhanced when the amount of ΔT increases.

In order to study the effects of other parameters such as strength of external electric field, we consider two more types in which the amount of E is increased compared with micro-mixer types in Fig. 5a and b. Fig. 5c shows the effect of increasing the amount of E on the flow pattern for micro-mixer in Fig. 5a. Obviously, the vortices formed near the walls of the micro-channel are disappeared. It is noteworthy that a weak chaotic flow pattern still remains despite vortices are eliminated due to increasing the amount of E. Fig. 5d shows the flow pattern when the amounts of both E and ΔT are increased. Surprisingly, a comparison between Fig. 5c and d shows that increase of ΔT does not strengthen the chaotic flow pattern while chaotic characteristic of flow field increases with ΔT for micro-mixers in Fig. 5a and b.

Based on what we presented for the modified Nernst–Planck equation (Eq. (9)), it seems that the temperature gradient could act as a source term similar to internal electric potential gradient for ion migration. Fig. 6 shows the non-dimensional ion species concentration distribution for micro-mixers of Fig. 5 at two planes A and B (Fig. 1). Considering the design of micro-mixer scheme A (Fig. 1), it can be found that the upper and lower edge of both planes A and B are placed on the red and blue blocks, respectively. For both planes, the $C_{Na^+}/n_{i\infty}$ and $C_{Cl^-}/n_{i\infty}$ are approximately equal to unity for $0 < y/H < 0.6$. The main reason in favor of this fact is that since the lower microchannel wall in these two planes is blue block ($\psi = 0.0$ and $T = T_{in}$) and the flow regime has low amount of Reynolds number, one cannot mention an effective factor such as migration or advection which could disturb the initial equilibrium state of ions species concentration in this region ($0 < y/H < 0.6$). On the other hand, Fig. 6a and b shows that closing to the upper wall microchannel would disturb the equilibrium state of initial ion concentration due to the presence of red block ($\psi = \zeta_{wall}$ and $T = T_{wall}$). As a result, for $0.6 < y/H < 1$, one can find that $C_{Na^+}/n_{i\infty} \geq 1$ and $C_{Cl^-}/n_{i\infty} \leq 1$.

Considering temperature effects on the distribution of ion species concentration, Fig. 6a and b shows that for both planes A and B near the red block, increase of ΔT has contrary effect on distribution of Na^+ and Cl^-. As a matter of fact, if ΔT increases, the amount of $C_{Na^+}/n_{i\infty}$ decreases considerably while the amount of $C_{Cl^-}/n_{i\infty}$ increases for plane A. On the contrary, as Fig. 6a and b shows, for plane B, if ΔT increases, the amount of $C_{Na^+}/n_{i\infty}$ increases and $C_{Cl^-}/n_{i\infty}$ decreases. This interesting effect of temperature gradient could be a balancing factor for the ion concentration ratio in EDL for both planes. It is worth mentioning that due to the presence of negative charges on the red block surface, the repulsion-attraction theory predicts higher concentration for counter-ions when temperature gradient is negligible. When ΔT increases, it seems that a secondary effective factor in addition to internal electric potential field causes ion species migration. From now on, we call this migration phenomenon as thermo-electrochemical migration. This term has appeared in the modified Nernst–Planck equation (Eq. (9)) as $(-eZ_iD_iC_i/KT^2)\nabla T \cdot \nabla \psi$.

Fig. 7 shows the schematic illustration of thermo-electrochemical migration phenomenon. It is shown that since the heaters placed on the red blocks are switched off (dashed line blue blocks), the counter-ions accumulate near the dashed line blue blocks while the accumulation of co-ions and counter-ions near the solid line blue blocks are equal due to the zero charge of them. However, when the heaters are switched on, the thermo-electrochemical migration phenomenon causes the migration of counter-ions from higher to lower temperature area while co-ions migrate from lower to higher temperature area.

Considering what we have mentioned above, one can conclude that thermo-electrochemical migration phenomenon causes the migration of counter-ions in opposite direction of $\nabla \boldsymbol{T}$ while co-ions migrate in direction of $\nabla \boldsymbol{T}$. As a main result for this phenomenon, it is anticipated that in regions which are affected by both red and blue blocks, due to higher amount of $\nabla \boldsymbol{T}$ and $\nabla \boldsymbol{\psi}$, we have powerful thermo-electrochemical migration near the blocks and as a result in red block region a balance of ions species is generated. Obviously, this phenomenon is indicated in Fig. 6a and b in which by increasing ΔT, the $C_{Na^+}/n_{i\infty}$ increases at plane B while at plane A,

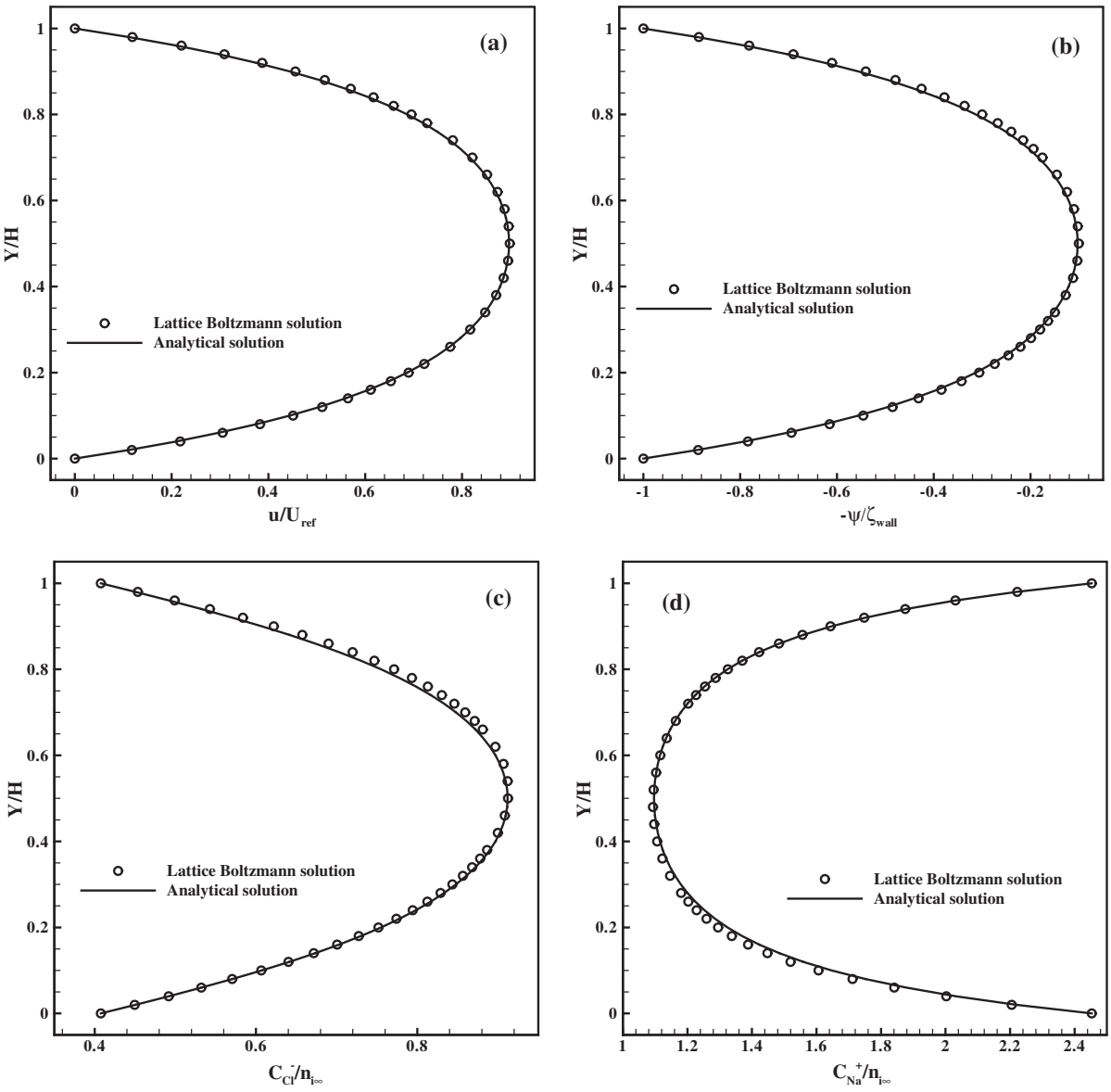

Fig. 4. Analytical solutions (solid line) and the PNP + NS coupled lattice Boltzmann results (circle symbols) for ideal EOF with $E_x = 1000$ V/m and $\zeta = -25$ mv. (a) Velocity profile. (b) Internal electric potential profile. (c) Cl^- Concentration profile. (d) Na^+ concentration profile.

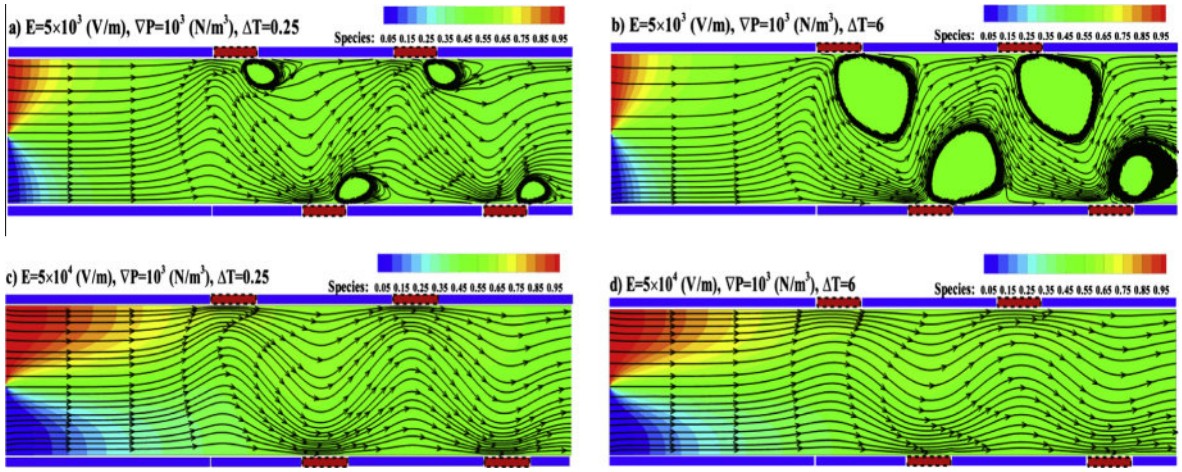

Fig. 5. Micro-mixer scheme A. Species contour and streamlines of velocity field. $\Delta T = \frac{T_{wall} - T_{in}}{T_{in}}$.

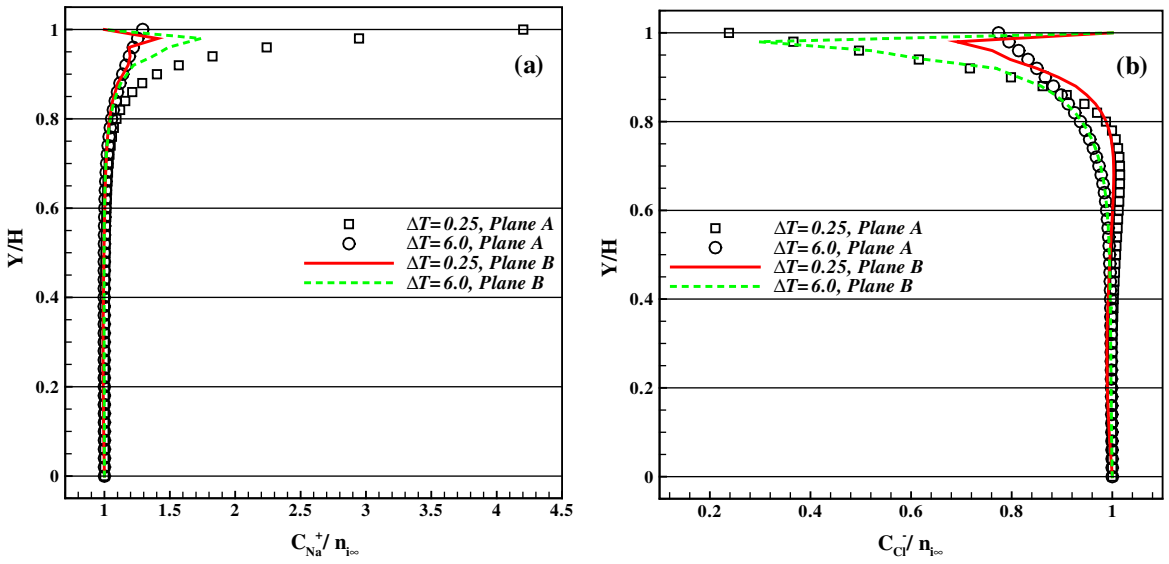

Fig. 6. Ions concentration distribution of micro-mixer scheme A for two planes A and B and two external electric field strength $E = 5 \times 10^3$ V/m and $E = 5 \times 10^4$ V/m.

the $C_{Na^+}/n_{i\infty}$ decreases. It should be noted that Fig. 6 presents the ion concentration distribution for four types of micro-mixer scheme A (Fig. 5).

Based on the electrical body force definition $F_e = \rho_e(E - \frac{\partial\psi}{\partial x})$, one can conclude that both net electric charge density and gradient of internal electric potential field may have their own specific effects on velocity field. It should be noted that temperature gradient has primary effects on distribution of ions (Eq. (9)) and consequently, the distribution of ψ and ρ_e would be dependent on the distribution of temperature. Fig. 8 shows the electrical body force for four types of micro-mixer scheme A. Based on what we have described

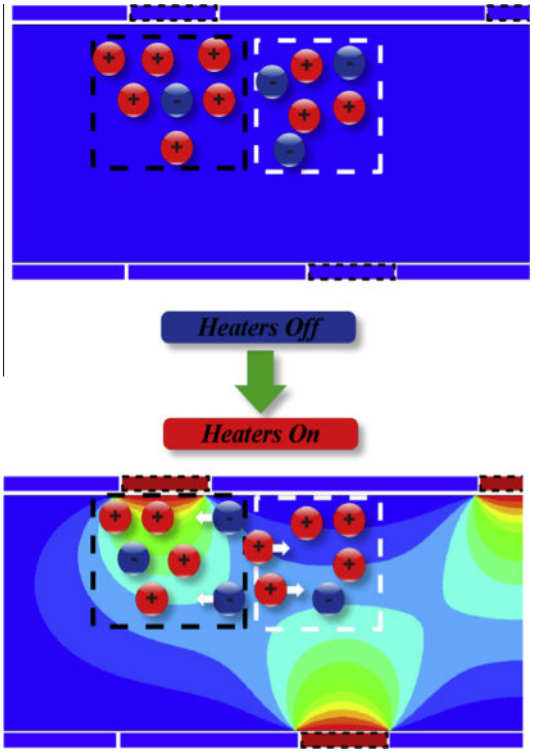

Fig. 7. Schematic illustration of the thermo-electrochemical migration phenomenon.

for Fig. 6, due to the equal amount of Na^+ and Cl^- for the range of $0 < y/H < 0.6$, the net electric charge density and thus the electrical body force would be approximately equal to zero. On the other hand, based on what we have mentioned for the thermo-electrochemical migration phenomenon, Fig. 8a and b shows that the electrical body force decreases at plane A when ΔT increases. It should be noted that the electrical body force is positive in regions which are affected by the red blocks. On the contrary, in regions which are affected by the blue blocks, we have negative body forces. In fact, the positive or negative electrical body force can be explained based on the sign of both net electric charge density and $-\partial\psi/\partial x$. As Fig. 6 shows, for the regions affected by red block, we have higher amount of C_{Na^+} than C_{Cl^-} due to the presence of negative charges on the block surface. So, ρ_e would be positive. In addition, $E - \partial\psi/\partial x$ is positive due to the high amount of external electric field. Therefore, it is concluded that the electrical body force in these regions would be positive. For the regions affected by blue blocks, as Fig. 6 shows, the net electric charge density is still positive. However, due to the zero zeta potential of the blue blocks, we have high amount of internal electric potential gradient ($\partial\psi/\partial x$) in a boundary region between red and blue blocks. As a result, the amounts of both $E - \partial\psi/\partial x$ and electrical body force would be negative (Fig. 8).

Considering our discussions for both Figs. 6 and 8, the main reason of why vortices form in boundary region of red and blue blocks has been uncovered. For this purpose, let us to assume a particle of fluid which is currently placed at plane A near the red block. A positive amount of electrical body force is exerted on this particle and the particle starts moving to the right side. On the other hand, in plane B, the negative amount of body force impels the particle in this region to move to the left side. When the assumed particle reaches this region (region with negative body force), naturally it would tend toward the central line of microchannel. This positive and negative amount of electrical body force in boundary region of red and blue blocks, respectively, would be the main reason of vortices formation. As Figs. 6c, d and 8b show, increasing the amount of E would diminish vortices due to the increase of the positive electrical body force in regions affected by red block and decrease of the negative amount of electrical body force of regions affected by the blue blocks.

Fig. 9 shows the species contour and streamlines of micro-mixer scheme B which is based on the symmetrical arrangement of red blocks (Fig. 1). Similar to those mentioned for Fig. 5, we have

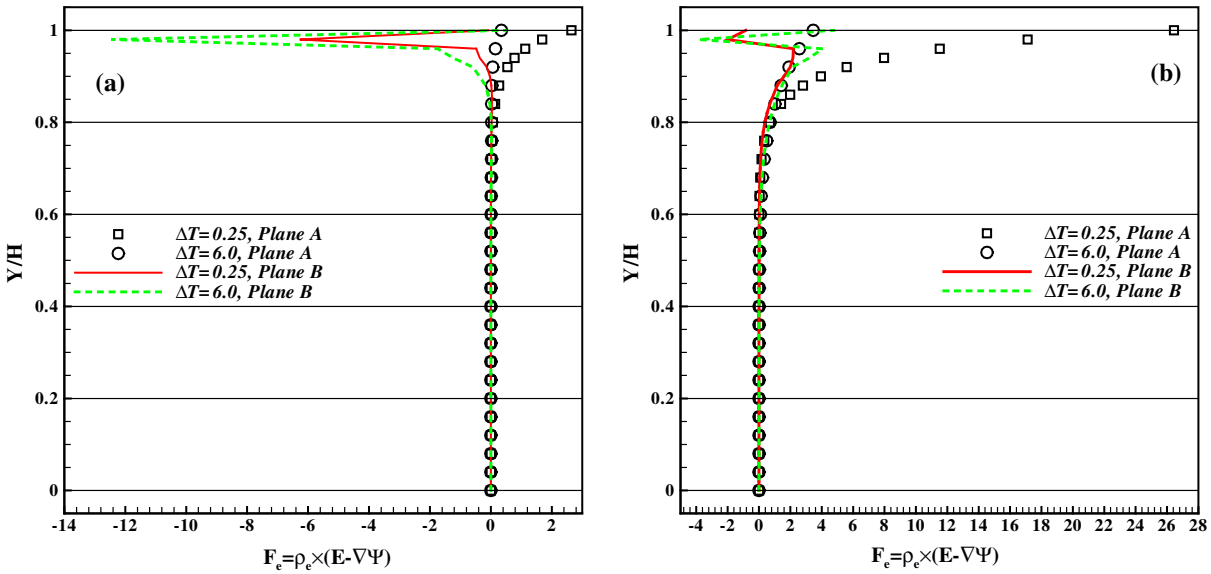

Fig. 8. Electrical body force distribution of micro-mixer scheme A for two planes A and B. (a) Electrical body force for micro-mixer scheme A with $E = 5 \times 10^3$ V/m. (b) Electrical body force for micro-mixer scheme A with $E = 5 \times 10^4$ V/m.

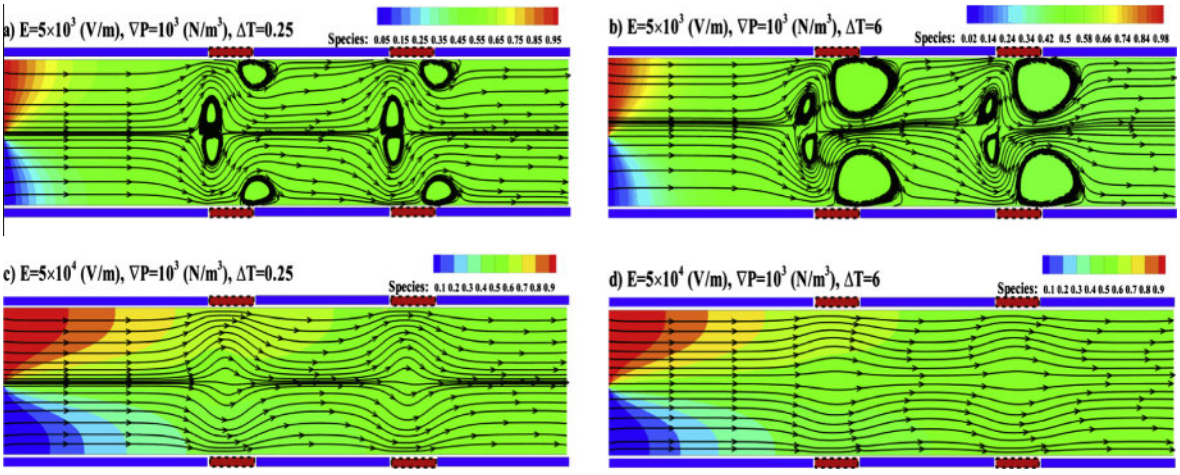

Fig. 9. Micro-mixer scheme B. Species contour and streamlines of velocity field.

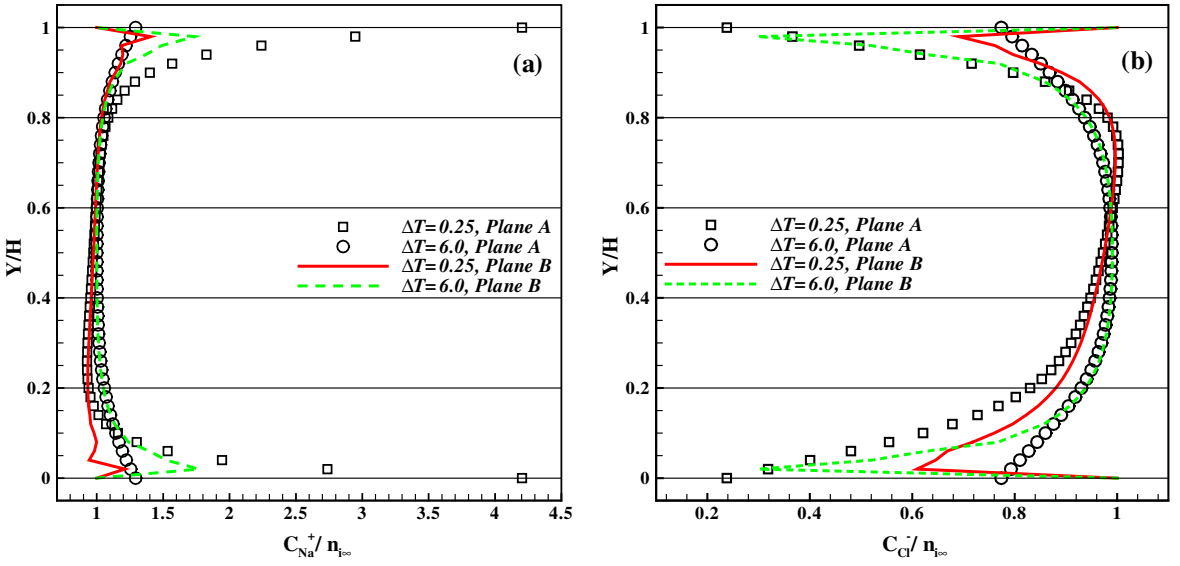

Fig. 10. Ions concentration distribution of micro-mixer scheme B for two planes A and B and two external electric field strength $E = 5 \times 10^3$ V/m and $E = 5 \times 10^4$ V/m.

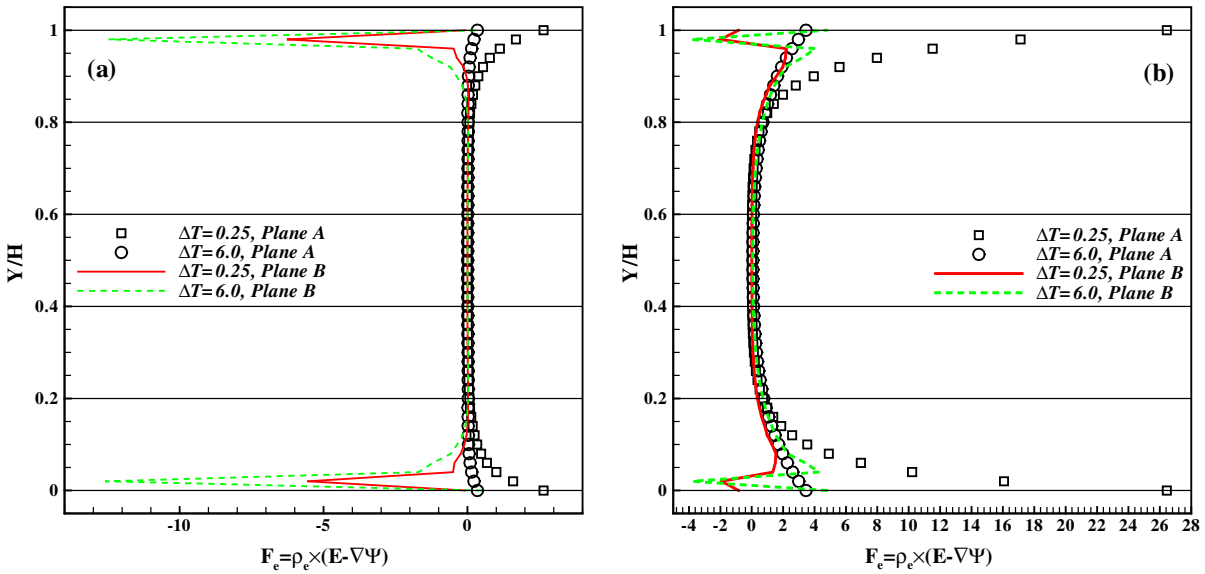

Fig. 11. Electrical body force distribution of micro-mixer scheme B for planes A and B. (a) Electrical body force for micro-mixer scheme B with $E = 5 \times 10^3$ V/m. (b) Electrical body force for micro-mixer scheme B with $E = 5 \times 10^4$ V/m.

two amounts of Reynolds number as $Re = 1.08 \times 10^{-3}$ (for Fig. 9a and b) and $Re = 1.0642 \times 10^{-2}$ (for Fig. 9c and d). Comparing Fig. 5a and b with Fig. 9a and b, one can conclude that the asymmetrical design of red blocks could cause larger scale of vortices near microchannel walls. It is noteworthy that similar to those mentioned for micro-mixer scheme A (Fig. 5), for micro-mixer scheme B with increasing the amount of ΔT the power of chaotic flow regime increases due to formation of larger scale of vortices. Later, it will be indicated that mixing of species would be enhanced with increasing the temperature difference, ΔT (Fig. 14).

One significant difference between micro-mixer scheme A and scheme B is that for $Re = 1.08 \times 10^{-3}$ (Fig. 9a and b), twin central vortices created at the sections of red blocks. Same as those mentioned for Fig. 5, increase of the strength of external electric field E would make the vortices disappear (Fig. 9c and d).

Fig. 9 shows that the y-directional force which drives the flow field to the red block regions in micro-mixer scheme A (Fig. 5) emerges in micro-mixer scheme B. Fig. 9a and b shows that by increasing the amount of ΔT, both the scale of vortices and the chaotic flow regime are increased.

Fig. 10 shows the ion species concentration distribution for plane A and B. It should be noted that for micro-mixer scheme B, with increasing the external electric field strength, there is not any significant change in ion species concentration distribution. Since the upper and lower edges of two cross sections of micro-mixer scheme B (Fig. 1) are placed on red blocks, the surface charge is $\psi = \zeta_{wall}$ and based on the repulsion-attraction theory, the concentration of Na^+ is higher than that for Cl^- (Fig. 10a and b).

According to what we have introduced as thermo-electrochemical migration phenomenon (Fig. 6), Fig. 10 shows that this phenomenon is governed wherever we have $\nabla T \neq 0.0$ and $\nabla \psi \neq 0.0$ independently from micro-mixer scheme. As the same as those we mentioned for micro-mixer scheme A, for plane A, when temperature difference increases, the amount of $C_{Na^+}/n_{i\infty}$ decreases while the amount of $C_{Cl^-}/n_{i\infty}$ increases all the while for plane B the amount of $C_{Na^+}/n_{i\infty}$ increased and $C_{Cl^-}/n_{i\infty}$ decreased. Fig. 10a and b shows that the presence of red blocks at the top and bottom edge of two mentioned planes causes wider area of microchannel deviate from the equilibrium state of ion species.

Fig. 11 shows the electrical body force distribution against microchannel width for two planes of micro-mixer scheme B. The reason for vortices formation in micro-mixer scheme A (Fig. 8) can be properly applied to in micro-mixer scheme B (Fig. 11).

Fig. 12 shows the species contour and streamlines of micro-mixer scheme C. According to what we have presented (Fig. 1),

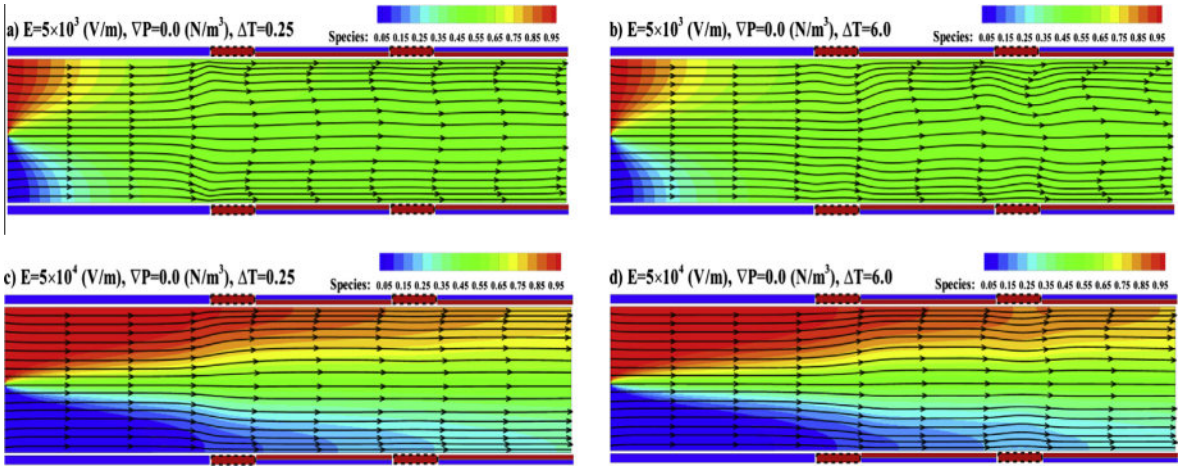

Fig. 12. Micro-mixer scheme C. Species contour and streamlines of velocity field.

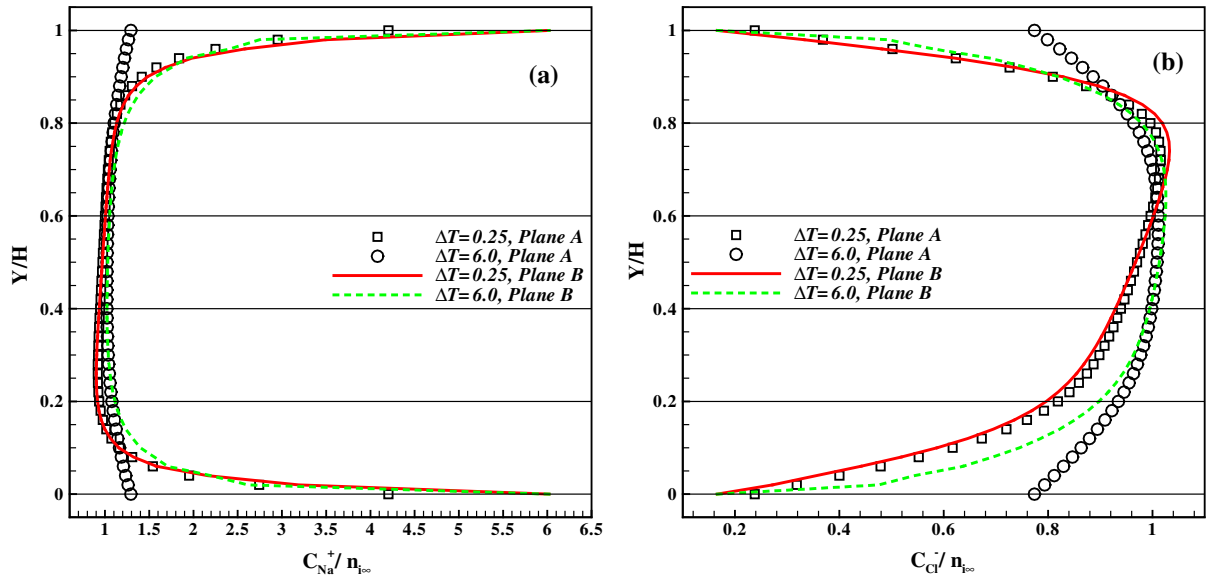

Fig. 13. Ions concentration distribution of micro-mixer scheme C for planes A and B and two external electric field strength $E = 5 \times 10^3$ V/m and $E = 5 \times 10^4$ V/m.

the main difference between micro-mixer scheme C with other micro-mixers is that we have activator blocks (red–blue blocks, blocks with $\psi = \zeta_{wall}$) between red blocks. Two amounts of Reynolds number are $Re = 1.062 \times 10^{-3}$ (Fig. 12a and b) and $Re = 1.062 \times 10^{-2}$ (Fig. 12c and d). A comparison between Fig. 12a and b shows that similar to micro-mixers scheme A and B, with increasing the amount of temperature difference ΔT, one can anticipate that the power of chaotic flow pattern is increased. Fig. 12c and d shows that with increasing the amount of external electric field strength E, the power of chaotic flow pattern decreased. Considering previous results of micro-mixer schemes A and B, this is an expected phenomenon which is occurred for micro-mixer scheme C.

Fig. 13 shows the ion species concentration distribution of micro-mixer scheme C for two mentioned planes against the width of microchannel. It is noteworthy that the thermo-electrochemical migration phenomenon would act as an effective role in migration of ions species when we have higher amount of internal electric potential field gradient, $\nabla\psi$, which could be reached due to temperature gradient or zeta potential-patterned walls. Fig. 13a and b shows that for plane A due to the higher amount of ∇T and being near neutral block (blue block), we would expect to have higher amount of $\nabla\psi$. As a result, it could be found that the thermo-electrochemical migration phenomenon decreases $C_{Na^+}/n_{i\infty}$ and increases $C_{Cl^-}/n_{i\infty}$. On the other hand, Fig. 13a and b shows that for plane B, there is not a powerful thermo-electrochemical migration phenomenon. One main reason in favor of this fact is that in this region the effect of zero zeta potential wall (blue blocks) is negligible. As a result, the amount of $\nabla\psi$ is small and thermo-electrochemical migration phenomenon which is related to $\nabla T \cdot \nabla\psi$ would be negligible.

Fig. 14 shows mixing length versus Reynolds number for micro-mixer schemes A, B and C. Mixing length is introduced as a factor for quantifying the mixing enhancement and defined as a length of microchannel before fully mixing of species. For this means, the relative concentration difference between upper and lower walls of the microchannel is defined as [34]:

$$\xi(x) = \frac{C_\Delta(x) - C'_\Delta(x)}{C_\Delta(x)} \tag{48}$$

where $C_\Delta(x) = \frac{\int_{H-\delta}^{H} C_s(x)dy}{\int_{H-\delta}^{H} dy}$ and $C'_\Delta(x) = \frac{\int_0^{\delta} C_s(x)dy}{\int_0^{\delta} dy}$. δ denotes a small distance from both upper and lower walls. In this study, mixing length is defined as the length when $\xi(x) < 0.03$. Fig. 14 shows that for all schemes of micro-mixers, the amount of mixing length increases significantly with Reynolds number. When the velocity is increased due to the increase of electrical body force, the species advection would be the dominant transport phenomena. Consequently, the mixing enhancement (lower amount of mixing length) would be highly dependent on the flow pattern. As a result, it seems that micro-mixers with larger size of vortices in higher amounts of Reynolds number could be treated as more efficient schemes.

Comparing micro-mixers scheme A, B and C, one can conclude that micro-mixer scheme A in $\Delta T = 6$ has the best mixing enhancement for both $Re = 1.08 \times 10^{-3}$ and $Re = 1.06 \times 10^{-2}$. It should be noted that in higher amount of Reynolds number, micro-mixer scheme C in $\Delta T = 0.25$ treats as the most inefficient micro-mixer among other schemes ($L_{mix}/H = 5.0$). Generally, considering micro-mixers scheme A, B and C, one can simply find that mixing

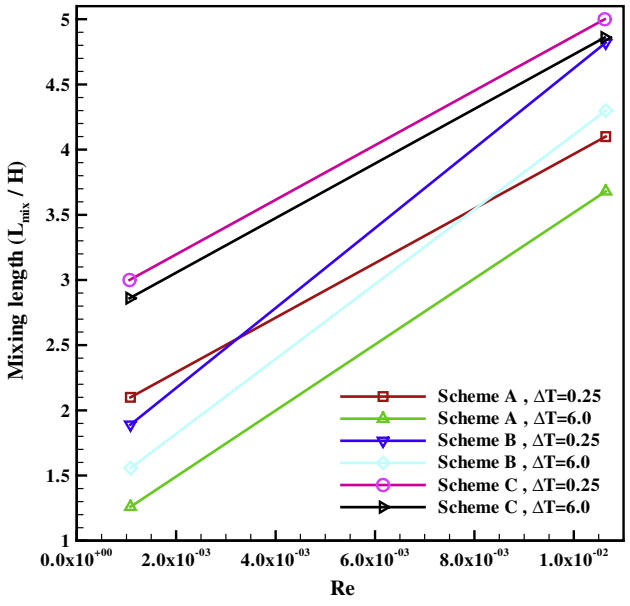

Fig. 14. Mixing length versus Reynolds number for three schemes of micro-mixers (Fig. 1).

of species is enhanced by increasing ΔT from 0.25 to 6.0. It should be noted that micro-mixer scheme A is the most effective scheme which enhances the species mixing about 39.8% when temperature difference increases from 0.25 to 6 At $Re = 1.08 \times 10^{-3}$ while micro-mixer scheme B and C enhances mixing of species by 17.6% and 5%, respectively. For $Re = 1.06 \times 10^{-2}$, increasing $\Delta T = 0.25$ to $\Delta T = 6$ enhances the mixing species of micro-mixer scheme A, B and C by 10.24, 10.78 and 2.8%, respectively. This could be a noticeable result for a micro-mixer which enhances the species mixing for Reynolds number on the order of 10^{-3}. As a ranking for the ability of mixing enhancement of micro-mixer schemes, Fig. 14 shows that micro-mixer scheme A performs as the most effective micro-mixer while micro-mixer scheme B and scheme C perform as the second and third effective micro-mixer, respectively.

6. Conclusions

This contribution has studied the mixing enhancement of low-Reynolds electro-osmotic flows in micro-mixers by temperature-patterned walls. The designed micro-mixers are based on symmetric and asymmetric arrangement of blocks with surface charges and higher temperature compared with inlet fluid. Since the fluid is non-isothermal, the conventional form of Nernst–Planck equation is not valid. As a result, it could be modified by adding a new migration term which is dependent on both temperature and internal electric potential gradient. This term causes the so-called thermo-electrochemical migration phenomenon. The Navier–Stokes, modified Nernst–Planck, Poisson, energy and advection–diffusion equations are solved numerically using an iterative process based on coupled lattice Boltzmann methods. Modeling results show that temperature gradient could emerge as a factor which controls the vortices scale and consequently the chaotic flow regime and as a main result the mixing enhancement of species. It is shown that the scheme with asymmetrical arrangement of blocks with non-zero charge and higher temperature has the most effective mixing enhancement when temperature difference increases specifically for low amounts of Reynolds number (order of 10^{-3}). The present results may help design of micro-mixers with improved ability of mixing species in microchannels.

Acknowledgments

This work is financially supported by the NSF grant of China (No. 51176089) and the Specialized Research Fund for the Doctoral Program of Higher Education of China (No. 20130002110077).

References

[1] C.C. Cho, C.J. Ho, C.K. Chen, Chem. Eng. J. 163 (2010) 180–187.
[2] R.H. Liu, M.A. Stremler, K.V. Sharp, M.G. Olsen, J.G. Snatiago, R.J. Adrian, H. Aref, D.J. Beeber, J. Microelectromech. Syst. 9 (2000) 190–197.
[3] J.M. Park, D.S. Kim, T.G. Kang, T.H. Kwon, Microfluidic Nanofluidic 4 (2008) 513–523.
[4] M.A. Ansari, K.Y. Kim, Chem. Eng. J. 146 (2009) 439–448.
[5] C.K. Chen, C.C. Cho, Chem. Eng. Sci. 63 (2008) 308–3087.
[6] S.P. Kee, A. Gavriilidis, Chem. Eng. J. 142 (2008) 109–121.
[7] D. Wang, J.L. Summers, P.H. Gaskell, Int. J. Comput. Math. Appl. 55 (7) (2007) 160–1610.
[8] M. Yi, H.H. Bau, Int. J. Heat Fluid Flow 24 (2003) 645–656.
[9] A.A. Deshmukh, D. Liepmann, A.P. Pisano, Continuous micromixer with pulsatile micropumps. Technical Digest of the IEEE Solid State Sensor and Actuator Workshop (Hilton Head Island, SC), 2000, pp. 73–76.
[10] I. Glascow, N. Aubry, Lab Chip 3 (2003) 114–120.
[11] L.H. Lu, K.S. Ryu, C. Liu, J. Microelectromech. Syst. 11 (2002) 462–469.
[12] N.T. Nguyen, Z. Wu, J. Micromech. Microeng. 15 (2005) R1–R16.
[13] Y.K. Lee, C. Shih, P. Tabeling, C.M. Ho, J. Fluid Mech. 575 (2007) 425–448.
[14] J.K. Wang, M.R. Wang, Z.X. Li, Mod. Phys. Lett. B 19 (2005) 1515–1518.
[15] Z. Tang, S. Hong, D. Djukic, V. Modi, A.C. West, J. Yardley, R.M. Osgood, J. Micromech. Microeng. 12 (2002) 870–877.
[16] T.J. Coleman, D. Sinton, Microfluidics Nanofludics 1 (2005) 319–327.
[17] M.H. Oddy, J.G. Santiago, J.C. Mikkelsen, Anal. Chem. 73 (2001) 5822–5832.
[18] S.M. Shin, I.S. Kang, Y.K. Cho, J. Micromech. Microeng. 15 (2006) 455–462.
[19] A. Alizadeh, J.K. Wang, S. Pooyan, S.A. Mirbozorgi, M. Wang, J. Colloid Interface Sci. 407 (2013) 546–555.
[20] J.K. Wang, M. Wang, Z. Li, J. Colloid Interface Sci. 296 (2006) 729–736.
[21] M. Wang, Q. Kang, J. Comp. Phys. 229 (2010) 728–744.
[22] J.K. Wang, M. Wang, Z. Li, Int. J. Therm. Sci. 46 (2007) 228–234.
[23] P. Dutta, A. Beskok, Anal. Chem. 73 (2001) 1979–1986.
[24] P.C. Lichtner, Principles and practice of reactive transport modeling. In: Material Research Society of Symposium on Proceedings, 353, 1995, pp. 117–130.
[25] D.Q. Li, Electrokinetics in Microfluidics, Academic, Oxford, 2004.
[26] S. Chen, G.D. Doolen, Annu. Rev. Fluid Mech. 30 (1998) 329–364.
[27] H.D. Chen, S.Y. Chen, W.H. Matthaus, Phys. Rev. A 45 (1992) R5339–R5342.
[28] J.K. Wang, M. Wang, Z.X. Li, Int. J. Therm. Sci. 46 (2007) 228–234.
[29] J.K. Wang, M. Wang, Z.X. Li, Commun. Nonlinear Sci. Numer. Simul. 13 (2008) 575–583.
[30] T. Inamuro, M. Yoshino, F. Ogino, Phys. Fluids 7 (1995) 2928–2930.
[31] C.H. Liu, K.H. Lin, H.C. Mai, C.A. Lin, Comput. Math. Appl. 59 (2010) 2178.
[32] A. D'Orazio, S. Succi, Future Gener. Comput. Syst. 20 (2004) 935–944.
[33] S.A. Mirbozorgi, H. Niazmand, M. Renksizbulut, J. Fluid Eng. 129 (2007) 1346.
[34] M. Wang, Z.X. Li, Int. J. Heat Mass Transfer 49 (2006) 1696–1702.